29th Congress of the International Council of the Aeronautical Sciences
St. Petersburg, Russia; September 7-12, 2014

EXPERIMENTAL AND NUMERICAL INVESTIGATION OF LOADING LEVELS AND DISTRIBUTIONS ON LOW PRESSURE TURBINE PERFORMANCE

A. R. Wadia
GE Aviation, Cincinnati, Ohio 45215, U.S.A.

Keywords: *Low Pressure Turbines, Loadings, Distributions*

Abstract

Experimental and numerical results from a study dealing with the effect of loading level and chord-wise loading distribution on low-pressure turbine (LPT) blade performance are presented. Only a single blade row is considered here, and the study is conducted in a stationary linear cascade that simulates the aero characteristics of a modern LPT design. The loading level and distribution are systematically varied by changing the number of blades (solidity), the stagger angle, and the unguided turning angle. The exit Mach number for this high-speed test is set at 0.64. The Zweifel number ranges from 1 (nominal lift) to 1.27 (high lift). The Reynolds number (based on chord and exit velocity) is varied from 70,000 to 350,000, a range that is broad enough to cover typical cruise and take-off conditions. While some data is taken near the end-walls, the primary focus of this study is on measurements at the mid-span. In addition to the profile loss, measurements include static pressure distribution on the blade surface and flow visualization. The data demonstrates increased suction side separation and consequent high losses as the loading level increases, the loading is moved aft, or the Reynolds number decreases. Three-dimensional CFD simulations corroborate these findings.

1 Introduction

In order to reduce cost and weight, low-pressure turbine (LPT) designers continue to strive for fewer turbine stages and fewer airfoils per row. The penalty with the use of such high-load / high-lift concepts is the potential risk of high aerodynamics losses depending on blade design and consequent loading distribution. As a result, there is significant motivation to obtain basic loss data to understand the underlying physical mechanisms that lead to these losses for various loading levels and distributions (front-, mid-, aft-). The impetus for the work presented in this paper is therefore obvious.

Turbine steady state losses are expressed as a sum of a profile loss and a secondary loss. The profile losses are related to "two-dimensional" flow mechanisms as exist near the mid-span away from the end-walls. The secondary losses, on the other hand, relate to complex "three dimensional" flows near the end-walls. Both the profile and secondary losses are affected by loading level and distribution.

The operational Reynolds number for a LPT can be low, especially at cruise. As a result, a significant forward portion of the airfoil suction surface is covered by a laminar boundary layer before it transitions to turbulence. If the Reynolds number is high, this laminar-turbulent boundary layer may remain attached to the suction surface. Otherwise, the laminar boundary layer may separate as it encounters the adverse pressure gradient near the aft portion of the surface. Often, the separation bubble is small and the flow re-attaches with transition to turbulence. However, under extreme circumstances, the separation bubble can be large and extend past the trailing edge.

The mechanisms of laminar-turbulence transition and separation on the suction surface are therefore key contributors to the profile loss. Clearly, excessive aft loading makes the suction surface vulnerable to flow separation and hence high profile losses.

Compared to an aft loaded blade, a front loaded blade shows lower profile losses and lesser sensitivity to operating conditions. However, it has been reported that front loading can lead to higher secondary losses.

Clearly, a blade designer must seek an optimal loading distribution, especially if the overall loading level is high. Other factors that may influence the decision include mechanical issues. For instance, aft loading may be preferred because of better stiffness characteristics.

Literature on the subject topic is extensive starting with the paper by Mayle [1] describing the role of laminar-turbulence transition in gas turbines. Notable recent studies relevant to the present investigation include the works of Popovic et al. [2], and Zoric et al. [3, 4] that shows high profile loss for aft loaded blades and high secondary losses for front loaded blades. The research group led by Hodson at Cambridge has pursued extensive research on this topic [5, 6], with particular emphasis on the effect of unsteady wakes from upstream rows on laminar-turbulence transition and separation. Their findings suggest that unsteady effects may perturb the laminar boundary thereby triggering transition and thence reducing flow separation and consequent losses. Similar conclusions are drawn by Tomikawa et al. [7] based on Large Eddy Simulations of flow through a LPT cascade. While these results may embolden a designer towards higher aft loading, it is for each organization to decide how much risk to build into their design practice.

On the analytical front, the subject topic has provided additional impetus towards the development of turbulence transition models that may be incorporated in computational fluid dynamics (CFD) codes. Notable recent efforts in this regard include the work of Praisner and Clark [8, 9] and Menter et al. [10, 11] about which more will be said later.

The work presented in this paper adds to the information available in open literature. In addition to its generic design value, the data obtained in this study is invaluable for developing validated CFD design tools.

2 Test Scope

Unlike solidity and loading level, which can be quantified in terms of the Zweifel coefficient, there is no direct numerical representation of the chord-wise loading distribution. Given a loading level, a blade designer usually manipulates blade orientation and geometry to achieve the desired distribution. Two quantities that play an important role in determining the loading distribution are the stagger angle and the unguided turning angle (UGT). These angles are defined in **Error! Reference source not found.**. As shown, the stagger angle is the angle between the line joining the leading and trailing edge to the engine axial direction. The unguided turning angle is the amount of turning that the fluid must undergo over the rear portion of the blade extending from throat to the trailing edge (the term unguided referring to the fact that there is no adjacent blade in this region to guide the turn). Low stagger and high unguided turning push the loading back and make the blade aft loaded. Alternately, high stagger and low unguided turning make the blade front loaded. While designing a blade, a designer usually attempts to keep these angles within a range prescribed by some established design practice.

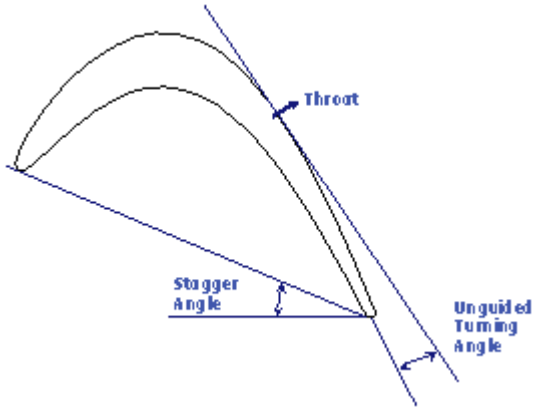

Figure 1: Illustration of stagger angle, unguided turning angle and throat location for an LPT blade.

In the present study, a total of six geometries were investigated, of which one group of three have high lift (Zweifel = 1.27),

and the other group of three have nominal lift (Zweifel = 1). The "incompressible" Zweifel number (Zw) is defined as:

$$Zw = 2\,(s / C_x)\cos^2(\beta_2)\,[\tan(\beta_1) - \tan(\beta_2)] \qquad [1]$$

Where s is the blade-to-blade spacing (pitch), C_x is the axial chord, and β_1 and β_2 represent the inlet and exit angles, respectively (in this case $\beta_1>0$ and $\beta_2<0$).

Within each group, the three geometries correspond to a "baseline" loading distribution, an aft- loaded distribution (lower-stagger / higher-UGT) and a front loaded distribution (higher-stagger / lower-UGT). For discussion hereon, each configuration will be identified by three letters of which the first two, HL- or NL-, designate *h*igh-*l*ift or *n*ominal-*l*ift respectively, and the third letter, –B, -A, or –F indicates *b*aseline, *a*ft, and *f*ront loading distributions, respectively.

All six geometries are run at the fixed inlet angle of 46.7 degrees fixed exit angle of -62.7 degrees and fixed inlet-total to exit-static pressure ratio of 1.32 (exit ideal Mach number ~ 0.64). Further, all blade geometries have the same axial chord. The blade- height to axial-chord ratio is 3.67.

Other parameters for the six cases are listed in Table 1. As will be observed, in terms of C_x/s, the solidity difference between the two groups is approximately 15 %, and, within each group, the change in stagger and UGT is plus/minus 7 degrees corresponding to different loading distributions. In the design world, the true chord C is often used instead of axial chord C_x. C and C_x are related to the stagger angle γ by the relation

$$C_x = C * \cos(\gamma) \qquad [2]$$

Whereas stagger angle is a fairly independent parameter, unguided turning is somewhat linked to solidity. For instance, holding all else fixed, if the blade spacing is reduced (i.e. solidity increased), unguided turning would reduce. This is the reason why the overall level of UGT is 7 degrees less for the nominal lift group compared to the high lift group.

It should also be noted that in the nominal solidity group, the front loaded case was chosen to have higher solidity compared to the other two cases. This was done intentionally in order to make this case more reflective of a design of practical interest.

Table 1: Aerodynamic Parameters

Geometry	Cx/s Cx=Axial Chord s=pitch	Zweifel	Stagger Angle (deg)	Unguided Turning Angle (deg)
HL-B	1.004	1.269	22.64	27.62
HL-A	1.004	1.269	15.90	34.29
HL-F	1.004	1.269	29.64	21.10
NL-B	1.155	1.104	22.65	20.51
NL-A	1.155	1.104	15.63	27.40
NL-F	1.264	1.009	29.65	10.69

2.1 Reynolds Number

Two Reynolds numbers are customarily used in literature: a Reynolds number (Re) that is based on the true chord C, and a Reynolds number (Re_{axial}) that is based on the axial chord C_x. In view of Equation [2], the two are related by:

$$Re = Re_{axial} / \cos(\gamma) \qquad [3]$$

In the present study, Re_{axial} = 134,000 (Re = 146,000) is representative of cruise (high altitude) conditions, while Re_{axial} = 247,000 (Re = 268,000) is reflective of take-off.

2.2 Design Loading Distributions (MISES)

The blades were designed by iterating on several geometry control parameters with continual monitoring of the overall flow and surface Mach number distribution as computed by a 2D inviscid CFD solver. The final designs were then evaluated using MISES, a 2D boundary layer code with a turbulence transition model [12]. The inlet turbulence intensity for MISES analysis was assumed to be 2%. The loading plots produced by MISES are shown in Figure 2. M_{ideal} is the isentropic Mach number based on local static and inlet total pressure. The

upper curves are for suction surface (low static pressure / high Mach number) and the lower curves are for the pressure surface (high static pressure / low Mach number). The high lift (HL) and nominal lift (NL) results are shown on separate plots for clarity and ease of reading.

In each figure, black, red and blue curves represent baseline (-B), aft (-A) and front (-F) loading distributions. Aft loaded blades have higher peak Mach numbers and higher aft diffusion on the suction surface. The term aft diffusion refers to the Mach number drop (static pressure rise) from the peak location to the trailing edge. It is this aft diffusion, which, when it becomes excessive, can lead to flow separation on suction surface resulting in high losses. As the loading is moved forward, aft diffusion decreases.

The shape of the loading curve on the suction surface from the peak Mach number point to the trailing edge is important because it can indicate the presence of a separation bubble. When that happens, the curve tends to flatten out in the separation bubble region. Of all cases considered in Figure 2, MISES indicated separation only for the HL-A configuration.

If there are no losses (i.e. on an inviscid basis), the area between the pressure and suction surface loading curves is representative of the overall lift and solidity. As a result, the enclosed area is higher in Figure 2a (high-lift / low-solidity) compared to Figure 2b (nominal-lift / higher-solidity). Within Figure 2a, all curves have the same solidity and hence the enclosed area is nearly the same for all cases. Thus, in this case, as the loading is increased in the rear (aft), it decreases near the front and vice-versa. For Figure 2b, it may be recalled from Table 1 that while cases NL-B and NL-A have equal solidity, the solidity for case NL-F is even higher. This is clearly reflected by the enclosed areas.

Unless there is a major change in separation characteristics, the chord wise loading distribution is not extremely sensitive to the Reynolds number. Hence, the plots shown in Figure 2 would be applicable unless there is significant flow separation.

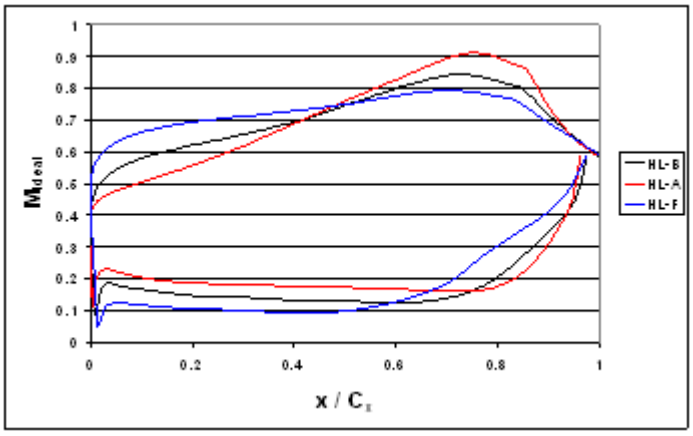

Figure 2a: Blade surface Mach number distributions calculated by MISES for the High Lift (HL) blades (Re_{axial}=134,000).

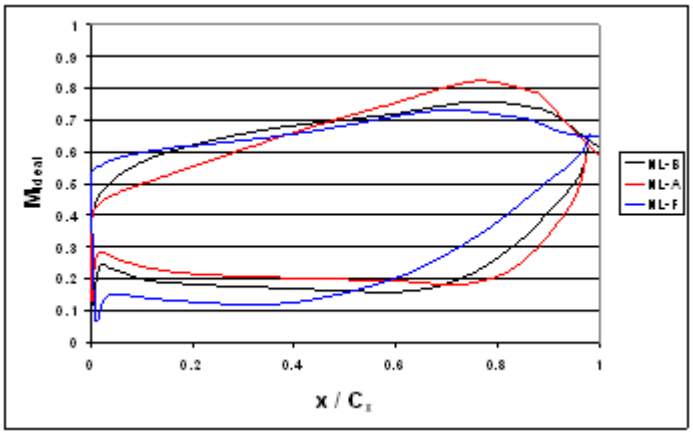

Figure 2b: Blade surface Mach number distributions calculated by MISES for the Normal Lift (NL) blades (Re_{axial}=134,000).

3. Experimental Set-up and Instrumentation

All tests were performed in a variable Reynolds number, transonic cascade wind tunnel. The facility is designed to operate as a "pull-through" wind tunnel, using an air ejector to pull ambient air through the flow path.

3.1 Test Facility Description

The motive air for the ejector is supplied by two 3,500-gallon air receivers and is regulated by a pneumatically controlled valve. This supply of air is capable of operating the wind tunnel at steady state conditions for ten seconds duration. A schematic of the facility is

presented in Figure 3a. An image of the cascade of blades can be found in Figure 3b.

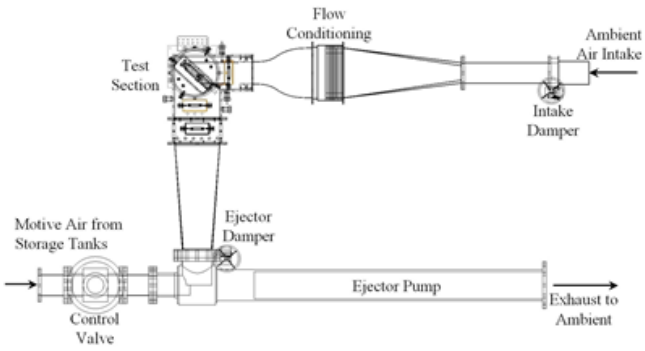

Figure 3a: Schematic of variable Reynolds number, transonic cascade facility.

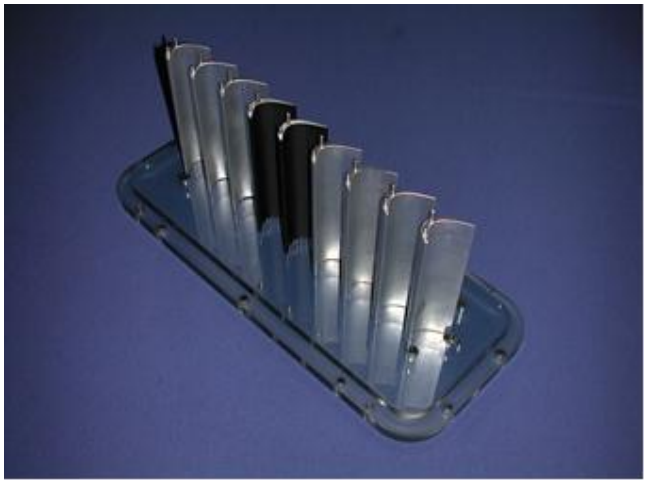

Figure 3b: Image of a cascade of LP-turbine blades

Reynolds number variation is achieved by controlling the inlet total pressure (density) via a damper at the air intake. This allows for absolute inlet total pressures ranging from a maximum of slightly below atmospheric to a minimum below 1 psia. A second valve, located downstream of the test section at the ejector intake controls the amount of suction created by the ejector. Together, these two valves provide independent control of the test section Mach and Reynolds numbers. The size of the test section was able to accommodate nine 1.51-inch axial chord length models of the three high-lift designs. For the higher solidity NL-B and NL-A geometries the cascade consisted of 10 blades and for the NL-F geometry 11 blades were used. At the design pressure ratio of 1.32, the facility was able to reproduce Re_{axial} numbers from approximately 75,000 to 350,000, which is more than adequate to cover the typical range of operation of a LPT blade from take-off to cruise.

3.2 Instrumentation

Test conditions were quantified using a single inlet Kiel probe to measure the inlet total pressure, three inlet static pressure taps and nine exit static pressure taps. All static pressure measurements were taken with pressure taps located on the endwalls of the tunnel. The inlet taps were equally spaced in the pitch-wise direction across the middle two passages at an axial location equal to one axial chord length upstream of the leading edge of the models. The exit taps were located at a distance equal to 33% of the axial chord downstream of the trailing edge plane and covered the middle four passages of the cascade. A diagram showing the locations of these measurements is illustrated in Figure 4.

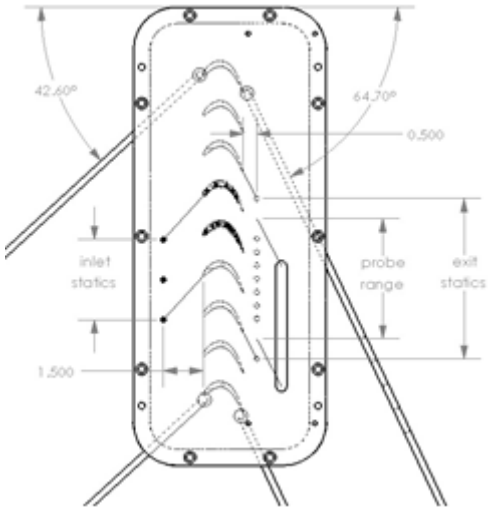

Figure 4: Cascade test section layout with the measurement locations.

The upstream Kiel probe was inserted a third of the span-wise height into the flow, far enough to be outside of the boundary layer but not so far that the wake of the probe might influence transition at the mid-span. The exit total pressure and flow angle distributions were

measured by a three-hole probe that was traversed across one pitch of the cascade at the mid-span. The traverse was taken along a path parallel to the cascade angle and located at a distance equal to 33% of the axial chord downstream of the trailing edges. From these measurements, the pressure ratio and Reynolds number were determined. The pressure ratio is defined as the ratio of the time averaged inlet total pressure, as measured from the inlet Kiel probe, to the time and area averaged exit static pressure, as measured from the exit static taps.

As mentioned earlier, the Reynolds number is based on the conditions at the exit of the cascade. Sutherland's law was used to estimate the viscosity. This requires the exit static temperature that was calculated using the inlet total temperature, exit Mach number and the assumption of no heat transfer through the tunnel walls. Density was calculated using this same temperature estimate and the area averaged exit static pressure from the end-wall static taps. The exit Mach number is calculated from the mass averaged exit total pressure and the area averaged exit static pressure. Finally the Mach number, combined with the local speed of sound, was used to calculate the exit velocity in the Reynolds number calculation.

3.3 Performance Calculations

All performance data were measured with the three-hole probe. With the three-hole probe, both total pressure and exit flow angle could be determined. For the purposes of measuring performance, the traverse covered a full pitch from y/pitch = –25% to y/pitch = 75% where y is the direction aligned with the cascade angle and the y/pitch = 0% line is defined as the line extending from the trailing edge of the center blade and along the design exit flow angle of 62.7 degrees. For clarity, this traverse path is shown in Figure 4.

The primary measure of performance used to evaluate the blades was mid-span blade row efficiency, also calculated as a loss parameter defined as one minus the blade row efficiency. The blade row efficiency is defined in Equation 4. The ideal exit Mach number was calculated using the time averaged inlet total pressure and a time and area averaged static pressure of the exit static taps located at y/pitch = -50, 0, 50 and 100%. The true exit Mach number was calculated using the same exit static pressure and a mass averaged total pressure taken from the traverse of the three-hole probe.

$$\eta_{bladerow} = \frac{V^2}{V_{ideal}^2} \qquad [4]$$

3.4 Blade Loading Measurement

Blade loading was measured using 17 static pressure probes on the suction surface of the center blade and 11 additional probes on the pressure side of the adjacent blade. An isentropic Mach number was calculated from these measurements using the inlet total pressure. A diagram of these pressure taps and a chart of their locations are shown in Figure 5. The diagram is for the NL-B configuration but the same axial locations were used for all six geometries with the exception of taps 7 and 8 on HL-A. These were moved to x/C_x = 0.436 and 0.595 respectively due to interference problems with the mounting pins. Due to fabrication errors not all of the pressure taps were operable in some of the models.

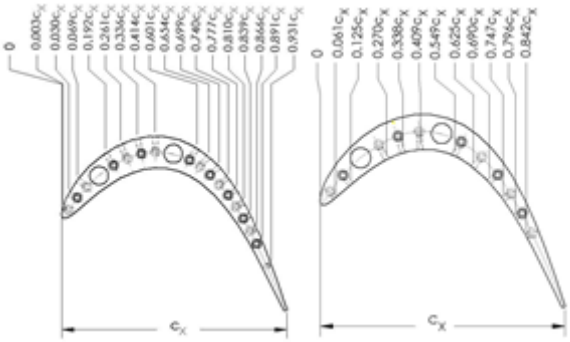

Figure 5: Location of blade suction and pressure side static pressure taps.

3.5 Flow Visualization

Flow visualization was performed by coating the surface of cascade models with a mixture of silicon oil and powdered, florescent paint pigment. The mixture was then allowed to flow over the surface of the blade during the

wind tunnel run, driven by the shear of the airflow. This is a particularly useful method for determine the separation and reattachment locations as well as for identifying secondary flow structures near the end walls. The best way to view the visualization is by video-taping the test event. That way, the direction of oil flow can easily be determined.

3.6 Inlet Velocity Profile Measurement

The inlet velocity profile was measured using pitot tube. Velocity data was also obtained as part of the hot wire turbulence data discussed next.

3.7 Turbulence Intensity Measurements

Hot-wire measurements were conducted to obtain the inlet turbulence intensity and length scale using a TSI 1240-20 X-probe sensor. The data was obtained 1.0 inch upstream of leading edge and 50% immersion. A DL716 digitizer was used with 50 kHz digitizing speed and data were obtained for 10 seconds. Data analysis indicated that most of energy came from below 5 kHz. Inlet turbulence intensity of 4.5% was measured. Turbulent length scale was estimated by measuring the decay of turbulence. Defined as

$$l = C_\mu \, k^{3/2} / \varepsilon \qquad [5]$$

the length scale l was estimated to be ~ 0.05 in. In Equation [5], k and ε represent the turbulent kinetic energy and dissipation rate respectively and C_μ is a constant = 0.09.

4. Test Results – Blade Loading Distributions

Figure 6a shows the measured loading distributions for the HL-B configuration. Several Reynolds number are considered including cruise (Re~146000), and takeoff (Re~268000). Also included is the analytical calculation based on MISES for the cruise condition.

The measured data agrees well with MISES at cruise condition. The flat shape of the loading distribution curve on the suction surface after the peak point is indicative of separation. Indeed, flow visualization did indicate a separation bubble on the suction surface at these conditions. The separation bubble was small and did reattach.

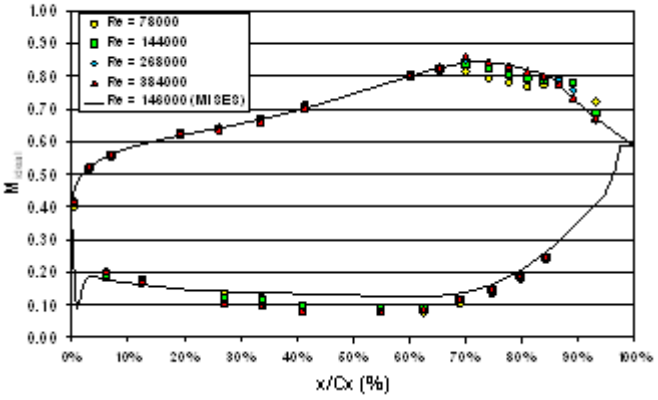

Figure 6a: Chord-wise loading distribution for High-Lift baseline (HL-B) configuration.

As the Reynolds number is increased to take-off and beyond, the flat (inflexion) region on the suction surface loading distribution curve reduces indicating less/no separation. Flow visualization at highest Reynolds number showed a fully attached flow.

The lowest Reynolds number shown (Re=78000) is not entirely academic because it could represent conditions in a small engine. As the loading plot data shows, the flow has a high propensity for separation under these conditions. This was confirmed by flow visualization which showed a large separation bubble on the suction surface without reattachment.

Loading distribution test data for the high-lift aft-loaded (HL-A) case are illustrated in Figure 6b. The high degree of flow separation on the suction surface at the two lower Reynolds numbers is evident in the data. Flow visualization at near-cruise Reynolds number (Re=142000) showed suction surface separation without reattachment. At the even lower Reynolds number (Re=760000), the onset of separation moved even further upstream and the flow did not reattach.

Loading distribution data for the two higher Reynolds number cases (Re=289000

being near-takeoff), do not indicate separation. Flow visualization for the Re=365000 indeed did not show any separation.

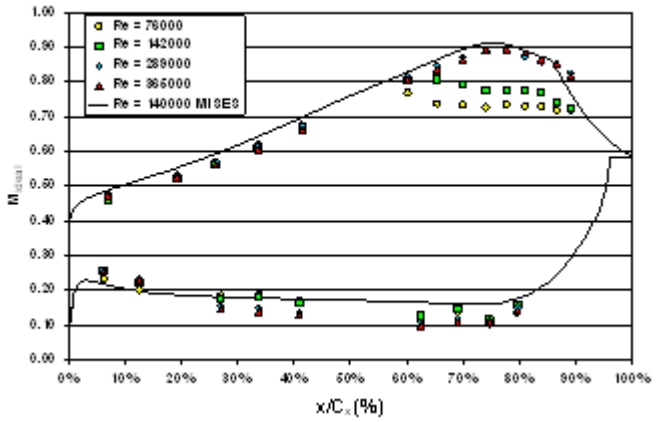

Figure 6b: Chord-wise loading distribution for High-Lift Aft-Loaded (HL-A) configuration.

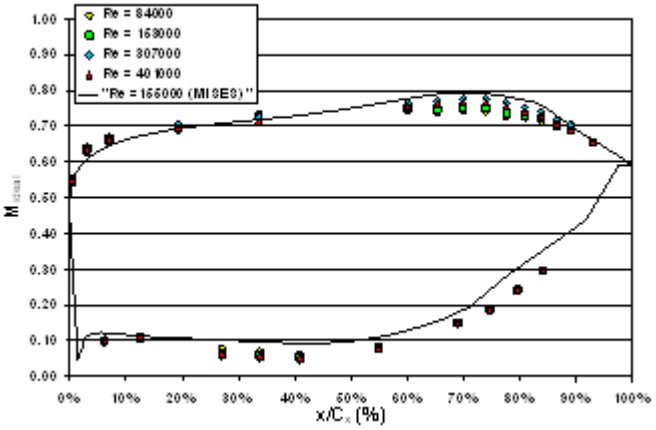

Figure 6c: Chord-wise loading distribution for High-Lift Front-Loaded (HL-F) configuration.

MISES did not predict large separation. As a result, MISES loading agrees well with high Re test data (which also had no separation) and departs from the low Re data (which indicated significant separation).

The data suggests that the combination of high-lift and aft-loading increases the possibility of suction side separation. As will be discussed later, such situations are accompanied by high losses.

Loading distribution results for high-lift front-loaded (HL-F) configuration are shown in Figure 6c. Shifting the loading forward reduces aft-diffusion and hence reduces the possibility of suction side separation. Like HL-B and HL-A, flow visualization indicated no flow separation at the two highest Reynolds numbers. However, unlike HL-B and HL-A, no flow separation was indicated at the design (cruise) Reynolds number as well which is a clear advantage of front loading.

The loading story is similar for nominal-lift (NL) cases except that by virtue of reduced overall loading, the peak Mach number and aft-diffusion are reduced compared to the high-lift cases discussed earlier. This would be evident by comparing high-lift data in Figures 6a, b, c with their equivalent nominal-lift data in Figures 7a, b, c. The most interesting cases to compare are the aft-loaded cases (Figures 6b and 7b). With higher solidity (Figure 7b), the blade can be sufficiently aft-loaded without major separation on the suction surface.

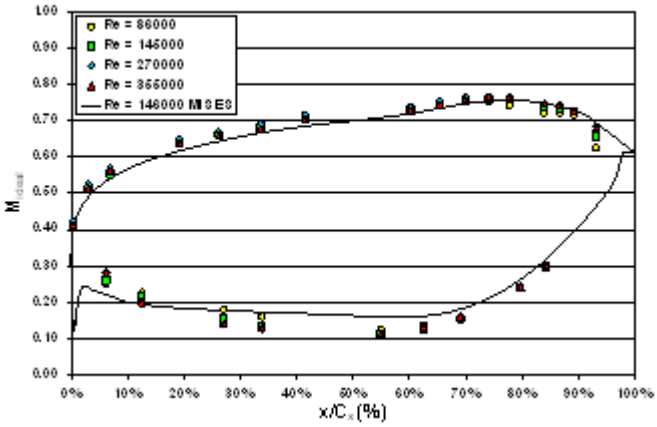

Figure 7a: Chord-wise loading distribution for Nominal- Lift Baseline (NL-B) case.

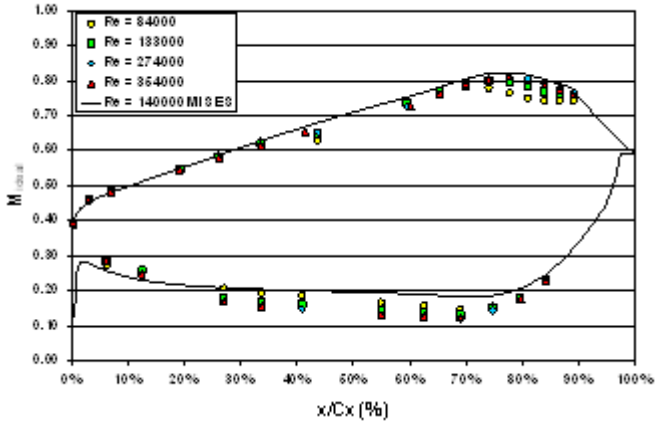

Figure 7b: Chord-wise loading distribution for Nominal-Lift Aft-Loaded (NL-A) case.

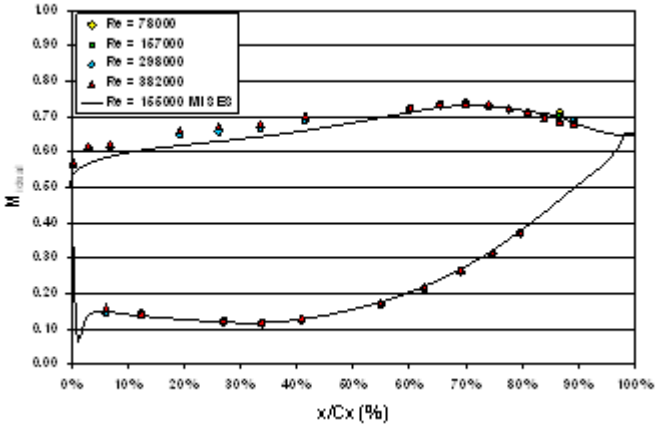

Figure 7c: Chord-wise loading distribution for Nominal-Lift Front-Loaded (NL-F) case.

Similar to the high-lift cases, flow visualization did not reveal any suction side separation for the nominal-lift cases.

As for HL-B, a small suction side separation was indicated by flow visualization for NL-B also. However, unlike the HL-B where the bubble re-attached, there was no reattachment for NL-B. This is probably due to the fact that in case of NL-B, the onset of separation was closer to the trailing edge, possibly not allowing it enough chord-wise distance to reattach.

Flow visualization for NL-A geometry closely resembled NL-B case. The separations were nowhere as aggressive as that for the equivalent HL-A.

The data suggests higher solidity combined with front loading makes NL-F the most benign case in terms of suction side separation. This was corroborated by flow visualization which indicated no separation except at the lowest Reynolds number.

4. Loss Measurements

From a practical standpoint, the most important quantity is the loss, defined as one minus the blade row efficiency given by Equation 4.

High-solidity/low-lift implies greater solid-fluid contact area (more blades) suggesting higher frictional losses. However, as seen in the loading distribution plots discussed earlier, low-solidity / high-lift leads to higher suction side velocities which also suggest increased losses. As a result, one may expect a mixed dependence of loss on solidity. Thus, starting from a very high solidity (low lift), one may expect the loss to decrease initially as the solidity is lowered (lift increased). Beyond a point, however, the loss will begin to rise again due to increased suction side velocity and altered boundary layer characteristics. Ultimately a point will be reached where the flow on suction side will separate resulting in even more rapid increase of loss.

The loss data for all configurations are presented in Figure 8. It is normalized by the loss for the high-lift baseline geometry (HL-B) at the cruise Reynolds number of 144000.

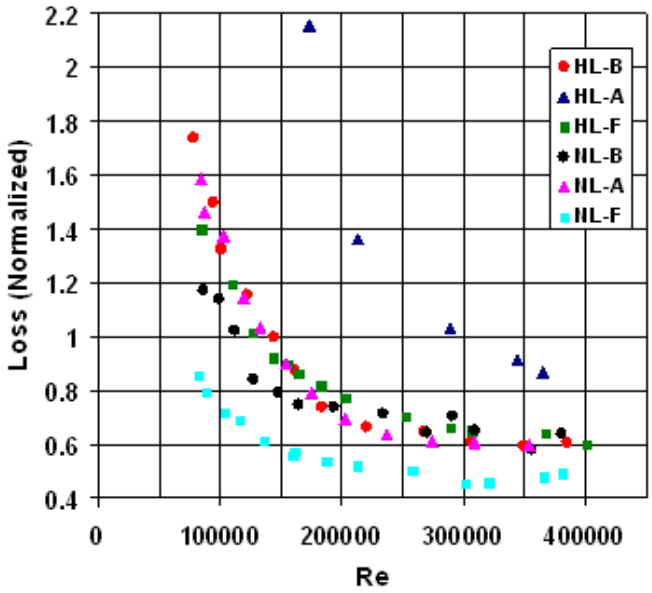

Figure 8: Loss (Equation [4]) normalized by loss for HL-B configuration.

The first observation on Figure 8 is the very high loss for the high-lift aft-loaded (HL-A) geometry. This is a consequence of very high degree of suction side separation due to excessive aft-diffusion for this case (recall discussion of loading plot for this case shown in Figure 6b). Lower the Reynolds number, greater the separation and losses and vice-versa. At the lowest At the Reynolds number of 76000, the normalized loss rose to a value of 6. Flow under these extreme conditions tended to become unsteady.

Loss numbers for the high-lift baseline (HL-B) and front-loaded (HL-F) are close. The

front loaded case appears to have slightly lower loss at low Reynolds numbers but a slightly higher loss at the higher Reynolds numbers.

For the nominal lift (higher solidity) also, the aft loaded case (NL-A) has higher losses compared to baseline because of larger suction side separation. As expected, this difference is higher at lower Reynolds number. However, the effect is not as dramatic as for the HL-A case. It may also be noted that NL-A losses are marginally lower than NL-B losses at higher Reynolds numbers.

Recall the nominal-lift front-loaded (NL-F) case has higher solidity compared even to NL-B and NL-A. This fact must be remembered in comparing the loss results. As expected, NL-F case has the lowest loss.

5. CFD Predictions

Test data obtained in this program was used for the validation of CFD codes, quite specifically, the calibration of turbulence transition models, which are needed to predict suction side separation. Recall, that a fully turbulent calculation will fail to predict suction side separation. Here, due to limited space, only a small sampling of CFD results is presented.

The transition model being pursued here is due to Menter et al. [10, 11]. It is based on two transport equations, one for intermittency and one for the transition onset criteria in terms of momentum thickness Reynolds number.

In the 3D CFD analysis, the above transition model may be used in conjunction with Wilcox's k-omega model [13] or Menter's SST model [14]. Additional modeling options relate to the choice of "turbulence limiters" which are needed to prevent excessive turbulence production in highly irrotationally strained turbo-machinery flows. Choices include the proposition of Kato and Launder [15], Durbin [16] and others.

Extensive CFD effort is currently underway to determine which set of modeling options gives best match with the cascade data reported in this paper. The findings are quite interesting and warrant a separate paper which may be forthcoming in future.

For cases that have little or no suction side separation, there is less difference between the predictions by different turbulent modeling options listed above. However, when there is significant suction side separation (low Reynolds number and / or high aft-diffusion), the predictions become more sensitive to modeling choices. While a final verdict has yet to be reached, the SST model [14] in conjunction with Durbin limiter [16] appears to have so far agreed best with the data.

Fig. 9 shows separation characteristics as predicted by the SST model with the Durbin limiter. Plotted are the contours of axial velocity Vx; in red indicating flow is from left to right (Vx>0) and blue indicating flow is from right to left (Vx<0). The size of the blue region is thus indicative of the size of flow separation. As Reynolds number and / or solidity increases, or as the loading is moved forward, CFD correctly predicted reduction of the size of separation bubble.

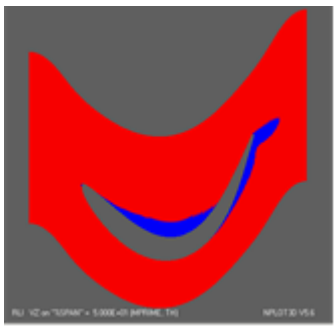

Figure 9: Contours of axial velocity (Vx) for HL-A configuration. Vx>0 is shown in RED. Vx<0 is shown in BLUE, implying separated flow. (Re = 140000, SST with Durbin limiter).

CFD loading distribution is compared for this configuration with data in Figure 10. The agreement of the CFD results with data is quite good. MISES (see black curve in Figure 2a) did not predict the separation and loading that well.

Figure 11 compares CFD loss predictions with test data for the high-lift baseline case (HL-B) for which the separation is not as severe. Once again the agreement is quite good.

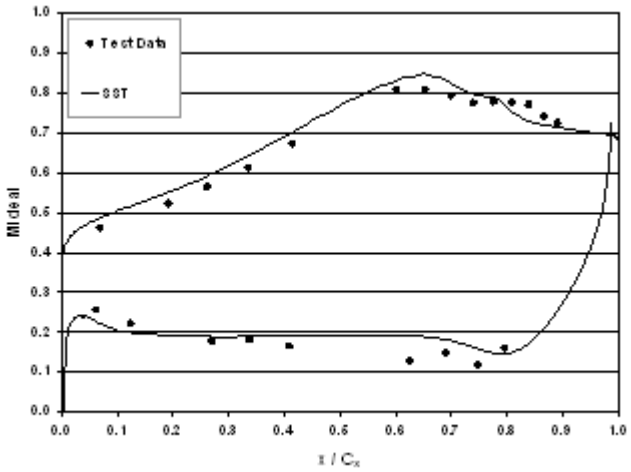

Figure 10: Comparison of the CFD loading distribution for HL-A configuration with test data. (Re=140000, SST with Durbin limiter)

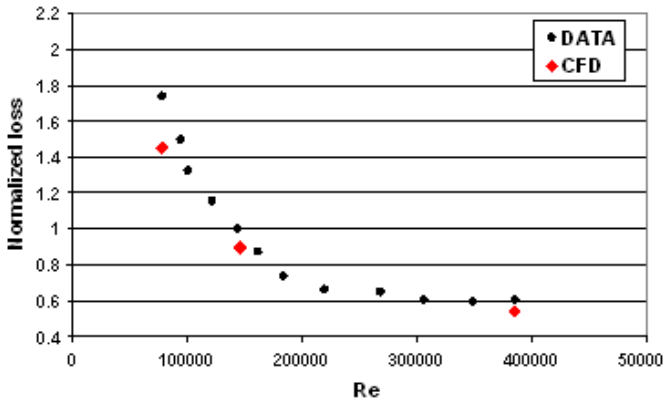

Figure 11: Comparison of CFD predicted loss for HL-B configuration with test data. (SST with Durbin limiter)

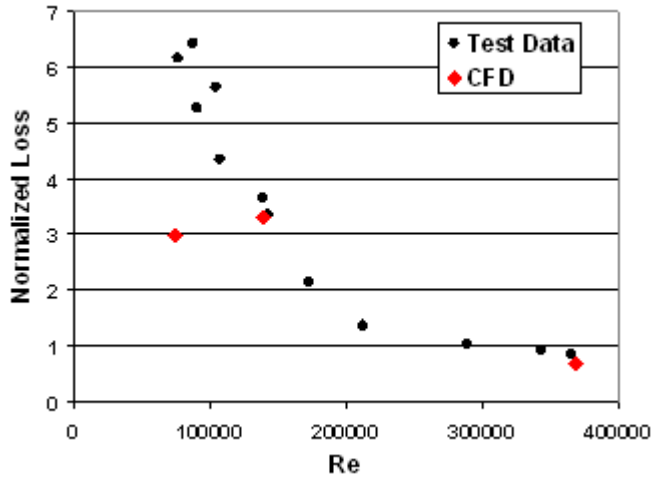

Figure 12: Comparison of CFD predicted loss for HL-A configuration with test data. (SST with Durbin limiter)

Figure 12 shows CFD loss predictions for the HL-A configuration. Again, the agreement is good. At the very low Reynolds numbers (Re < 100000), the disagreement is probably due to the fact that the flow was very highly separated and unsteady

6. Concluding Remarks

While high-lift (low-solidity) blades offer the advantage of low cost and weight, they also run the risk of high losses due to suction side separation. The issue of loading distribution thus becomes increasingly important for high-lift blades. Caution needs to be exercised in moving the loading aft for such high lift situations due to risk of flow separation and high losses. Recent advances in turbulence transition models for CFD codes appear promising in predicting some of the trends observed with high lift airfoils at low Reynolds numbers. However, further validation work is needed in order to identify the optimal modeling options.

7. References

[1] Mayle, R.E., "The Role of Laminar-Turbulent Transition in Gas Turbine Engines", ASME, J. Turbomachinery, Vol. 113, October 1991, pp. 509-537.

[2] Popovic, I., Zhu, J., Dai, W., Sjolander, S. A., Praisner, T. and Grover, E., "Aerodynamics of a Family of Three Highly Loaded Low-Pressure Turbine Airfoils: Measured Effects of Reynolds Number and Turbulence Intensity in Steady Flow", ASME paper GT-2006-91271.

[3] Zoric, T., Popovic, I., Sjolander, S. A., Praisner, T. and Grover, E., "Comparative Investigation of Three Highly Loaded LP Turbine Airfoils: Part I – Measured Profile and Secondary Losses at Design Incidence", ASME paper GT-2007-27537.

[4] Zoric, T., Popovic, I., Sjolander, S. A., Praisner, T. and Grover, E., "Comparative Investigation of Three Highly Loaded LP Turbine Airfoils: Part I – Measured Profile and Secondary Losses at Off-Design Incidence", ASME paper GT-2007-27538.

[5] Howell, R. J., Ramesh, O. N., Hodson, H. P., Harvey, N. W. and Schulte, V., "High Lift and Aft Loaded Profiles for Low Pressure Turbines", ASME paper GT-2000-261.

[6] Opaka, M. M. and Hodson, H. P., "Transition on the T106 LP Turbine Blade in the Presence of Moving Upstream Wakes and Downstream Potential Fields", ASME paper GT-2007-28077.

[7] Tomikawa, K., Horie, H., Iida, M., Arakawa, C., and Ooba, Y., "Parametric Surveys of the Effects of Wake Passing on High Lift LP Turbine Flows Using LES", ASME/JSME Fluids Engineering Conference, paper FEDSM-2007-37208.

[8] Praisner, T. J. and Clark, J. P., "Predicting Transition in Turbomachinery, Part I – A Review and New Model Development", ASME paper GT-2004-54108.

[9] Praisner, T. J., Grover, E. A., Rice, M. J. and Clark, J. P., "Predicting Transition in Turbomachinery, Part II – Model Validation and Benchmarking", ASME paper GT-2004-54109.

[10] Menter, F. R., Langtry, R. B., Likki, S. R., Suzen, Y. B., Huang, P. G., "A Correlation-Based Transition Model Using Local Variables: Part I – Model Formulation", ASME GT-2004-53452.

[11] Langtry, R. B., Menter, F. R., Likki, S. R., Suzen, Y. B., Huang, P. G., "A Correlation-Based Transition Model Using Local Variables: Part II – Test Cases and Industrial Applications", ASME GT-2004-53454.

[12] Drela, M., "MISES Implementation of Modified Abu-Ghannam/Shaw Transition Criteria", MIT Technical Report, 1995.

[13] Wilcox, D. C., Turbulence Modeling for CFD, Second Edition, DCW Industries, Inc., La Canada, California, 1995.

[14] Menter, F. R., "Two-equation eddy-viscosity turbulence models for engineering applications", AIAA Journal, Vol. 32, No. 8, pp. 1598-1605, AIAA Journal, Vol. 40, No. 2, pp.254-266, 2002.

[15] Kato, M. & Launder, B.E., "Modelling Flow-Induced Oscillations in Turbulent Flow Around a Square Cylinder", ASME FED, Vol. 157, pp. 189-199, 1993.

[16] Durbin, P. A., "On the k-e Stagnation Point Anomaly", Int. J. Heat and Fluid Flow, Vol. 17, pp. 89-90, 1996.

8. Copyright Statement

9. Contact Author Email Address

Mail to: aspi.wadia@ge.com